Slat Noise from an MD30P30N Airfoil at Extreme Angles of Attack

Filipe Ramos do Amaral[*] and Fernando Henrique Tadashi Himeno[†]
University of São Paulo, 13566-590 São Carlos, Brazil
Carlos do Carmo Pagani, Jr.[‡]
São Paulo State University, 13876-750 São Joao da Boa Vista, Brazil
and
Marcello Augusto Faraco de Medeiros[§]
University of São Paulo, 13566-590 São Carlos, Brazil

This study investigates the slat noise of a two-dimensional scaled, unswept, and untapered MD30P30N high-lift model. The experimental data refer to aeroacoustic and aerodynamic measurements in a closed-section wind tunnel for a wide range of angles of attack (from −6 deg up to the stall; approximately at 18 deg) and Mach numbers between 0.07 and 0.1. Three slat configurations (the original MD30P30N, another with a higher slat deflection, and one with smaller slat gap and overlap) are studied experimentally. The signal processing applied to the acoustic data involves conventional beamforming enhanced by two deconvolution algorithms, namely, DAMAS and CLEAN-SC. An original variation of the beamforming cluster approach that is based on the coherence level among microphone pairs is introduced, and it improves the results obtained by DAMAS. Below −2 deg and above 12 deg angles of attack, the slat noise is very small and mostly below the wind-tunnel background noise for all configurations. Between −2 and 12 deg angles of attack, the slat noise spectra are substantially affected by the slat configuration, although it always contains a dominant low-frequency content, a midfrequency broadband noise, and a single high-frequency broad peak. Within this range, the lower angles of attack display the strongest low-frequency narrowband peaks. In fact, at lower angles of attack, the low-frequency narrowband peaks scale with a Mach power above 10.

I. Introduction

THE substantial reduction in the turbofan noise emission achieved over the past decades has rendered the airframe noise of large commercial aircraft as a potentially important contributor to the overall noise during approach and landing procedures [1]. Hence, endeavors aiming at silent aircraft have also focused on airframe noise reduction. Among airframe components, landing gear and high-lift systems (trailing-edge flaps and leading-edge slats) have been identified as prominent noise contributors, however, their ranking depends on the aircraft model and high-lift configuration [2]. The flap tip can produce high-level localized sources; however, new designs that use moderate to low flap deflection tend to be quieter. The deployed leading-edge slats often span almost the entire wings and, as a consequence, may become the dominant airframe noise for such aircraft [3].

Slat noise has been studied from wind-tunnel measurements [4–7], numerical simulations [8–12], and flyover tests [13]: in all of which the upper slat trailing-edge appears as a potential region for noise emission. A limited number of unswept and untapered high-lift scaled models has been studied in the literature, e.g., the MD30P30N [14–16], the Boeing 777 two-dimensional (2-D) high lift [17], and energy-efficient transport [18,19]. All of these investigations identified three well-marked components in the slat noise spectra, which were observed in similar ranges of Strouhal numbers, namely, multiple low-frequency narrowband peaks, broadband noise ranging

from low- to midfrequencies and a single high-frequency broad peak beyond the broadband range. The source frequencies scaled with the size of the slat cove, and the noise level increased with the flow velocity raised to a power between four and six [19–21].

The MD30P30N is a well-researched configuration [6,14,15]. A limited number of studies systematically investigated the effect of slat configuration (namely, gap, overlap, and slat deflection) on noise emission [3,18,22,23]. Such studies clearly indicated that the slat configuration parameters could have a substantial impact on the noise spectra. In general, the low-frequency narrowband peaks were the dominant feature at lower angles of attack (AOAs); although, for some configurations, the high-frequency hump reached similar noise levels at higher angles of attack [23]. A number of studies reported the narrowband peaks were a low-Reynolds-number feature associated with the small scale of wind-tunnel models, and they were absent in the higher Reynolds numbers of real aircraft [2,18,19]. Investigations with a swept and tapered wing also produced slat noise spectra dominated by low-frequency multiple narrowband peaks. Such peaks were suppressed by the tripping of the boundary layer at the slat lower surface, before the slat cusp, leading to broadband slat noise spectra [24]. These results supported the argument that the low-frequency narrowband peaks were restricted to low Reynolds numbers. However, attempts at eliminating the narrowband peaks by tripping of the boundary layer for unswept or untapered high-lift models did not succeed [25,26], or they led to an increase in the narrowband peak level [16].

Previous research suggested a good aerodynamic performance was associated with high slat noise [22,23]. Nevertheless, this aspect deserves further attention because the studies of slat noise have almost entirely been conducted for the usual operational wing angles of attack, i.e., positive angles up to 10 deg [14,15,22,23]. Three-dimensional effects on the wing of a real airplane may cause the effective angle of attack to be substantially outside of such range for certain wing sections. Furthermore, circumstances may dictate an airplane to operate off its design approach and landing conditions. These circumstances motivated this investigation into the aerodynamics and aeroacoustics of the slat of a three-element high-lift model in a wide range of angles of attack, i.e., from −6 deg up to the stall close to 18 deg. Three slat geometrical configurations (i.e., the MD30P30N baseline, another with a 35 deg slat deflection, and one with a smaller gap and overlap than the original

*Ph.D. Student, Department of Mechanical Engineering; framaral@usp.br.
†M.Sc. Student, Department of Mechanical Engineering; fernando.himeno@usp.br.
‡Assistant Professor; carlos.pagani@sjbv.unesp.br.
§Associated Professor, Department of Aeronautical Engineering; marcello@sc.usp.br. Fellow AIAA.

a) Diagram of the three slat configurations tested　　　b) Deflection, gap, and overlap definitions
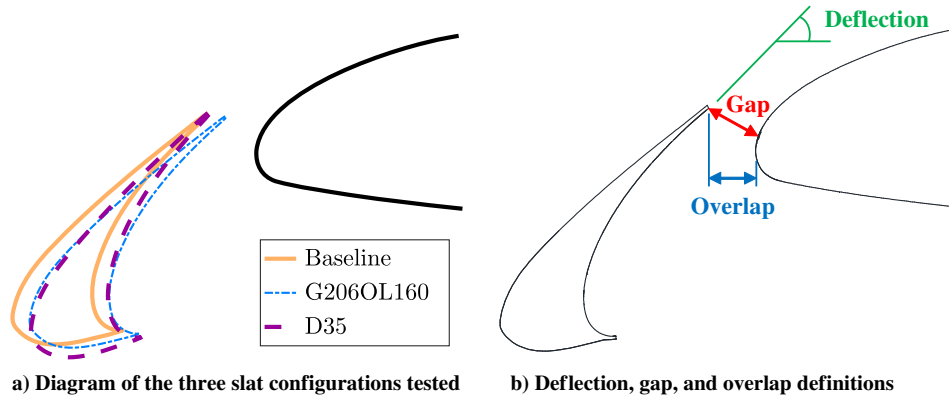
Fig. 1　Slat parameters definitions. The main element leading edge is shown on the right side and provides a position reference.

configuration) were tested. These configurations were selected from a study that investigated 10 different slat configurations [23], however in a restricted angle-of-attack operational range.

The experiments were performed in a closed-section wind tunnel, and acoustic measurements used a wall-mounted 62-element microphone array. A comparison between numerical and experimental aeroacoustic results in a closed-section wind tunnel suggests the experiments underestimated the noise at higher frequencies [7]. In fact, at higher frequencies, a severe coherence loss might lead to source level underestimation, particularly for wall-mounted microphone experiments [27]. In view of that, an original strategy was developed to prevent the coherence loss effects.

II.　Methodology

A.　Experimental Setup

The geometry of the MD30P30N high-lift airfoil model was the base for our experiments. It had a 500 mm chord in the stowed configuration and a 1300 mm span, and it was manufactured in SAE7075 aluminum alloy. Some parts of the slat and flap, at the middle span, were manufactured via rapid prototyping for enabling flexibility in the chordwise position of the pressure tappings, whereas the main element surface pressure tappings were directly drilled onto the aluminum alloy surface. Small brackets fixed the slat and flap configurations, i.e., their gap, overlap, and deflection angle were manufactured in SAE8640 steel. The model was centered on a turntable and fixed with small brackets. The slat chord was 15% of the model stowed chord. Three slat configurations were employed (Fig. 1), and their characteristics are shown in Table 1. The chord of the flap was 30% of the model stowed chord; and its gap, overlap, and deflection angle were 1.25%, 0.25%, and 30 deg, respectively, for all slat configurations tested.

The experiments were conducted in a closed-circuit wind tunnel at the University of São Paulo's São Carlos Engineering School. The tunnel had a closed test section of 1300 mm in height, 1700 mm in width, and 3000 mm in length; and it could reach velocities up to 34 m/s. The angles of attack based on the main element chord ranged between −6 and 18 deg for the baseline and G206OL160 configurations, and between 0 and 16 deg for D35 configuration. The freestream speeds U_∞ were 24, 27, 31, and 34 m/s for all configurations, whereas the Reynolds numbers based on the airfoil
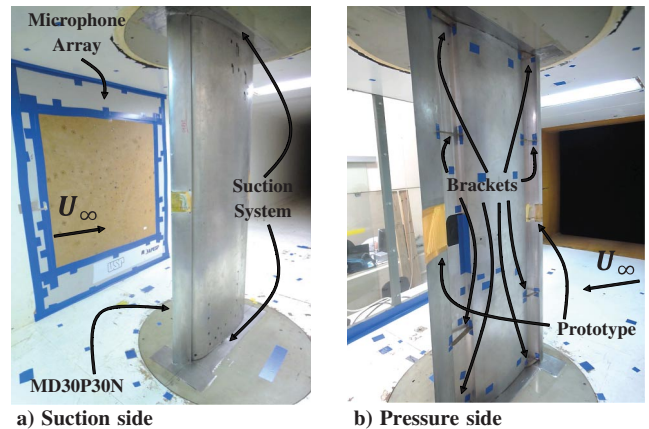

a) Suction side　　　b) Pressure side

Fig. 2　MD30P30N model installed in the wind-tunnel test section.

stowed chord were approximately from 7.06×10^5 to 9.62×10^5 and the Mach numbers approximately from 0.07 to 0.1. Figure 2 shows the model inside the wind-tunnel test section and the microphone array, and Fig. 3 displays a scheme of the model position relative to the array. More details on the position of the model relative to the microphone array, the turntable, and the test section walls were shown in [23].

The model instrumentation includes 143 static pressure tappings at midspan along a chordwise line, distributed on the slat, main element, and flap; and 40 pressure tappings along the span at two positions on the suction side of the main wing: one near its leading edge and another near its trailing edge [23]. The 40 pressure tappings monitored the two-dimensionality of the time-averaged flow over the model.

For a better two-dimensional flow, the wind-tunnel wall boundary layer was controlled by suction upstream of the slat and on the suction side of the main element; see Fig. 2. Before the actual experiment, a study was performed for adjusting the wind-tunnel wall boundary-layer suction level [7,28]. The suction was provided by a sidewall venting placed outside the tunnel, and its level was defined by the frequency of the sidewall venting controller [28]. The undesirable effects caused by the wind-tunnel wall boundary layer were associated with the lift of the model [29]. Therefore, no suction was required for the lower angles of attack tested, i.e., −4 and −6 deg, which generated no lift.

B.　Acoustic Data Postprocessing

In-house codes [7,23,28,30] implemented in a frequency domain, including the conventional beamforming technique, as well as deconvolution techniques, such as DAMAS (which stands for deconvolution approach for the mapping of acoustic sources) [31] and CLEAN-SC (which stands for CLEAN based on source

Table 1　MD30P30N slat configuration parameters[a]

Case	Deflection, deg	Gap, %	Overlap, %
Baseline	30	2.95	−2.50
D35	35	2.95	−2.50
G206OL160	30	2.06	−1.60

[a]Percentages are relative to the model stowed chord.
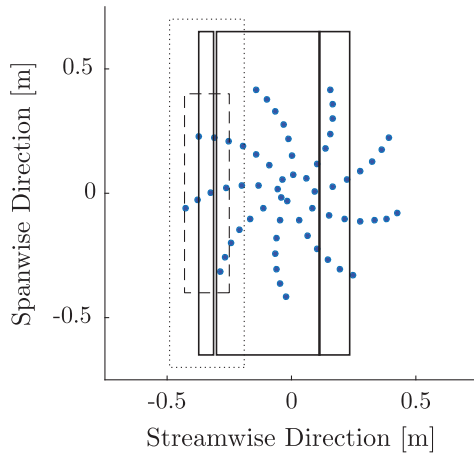
Fig. 3 Diagram containing projections of the airfoil model, microphone array, mesh domain and ROI.

Fig. 4 Array beamwidth and dynamic range assessed between 500 and 18,000 Hz.

coherence) [32], were employed for acoustic database postprocessing. The acoustic beamforming algorithm applied [33,34] assumed a spherical wave propagation under a free-field condition emanating from a distribution of uncorrelated monopole point sources. The uniform grid spatial resolution was defined as a function of the beamwidth for each frequency of interest [31]. Tests were performed to ensure the results' independence of the spatially integrated sources on the mesh resolution and domain size. More details on the algorithms implemented can be found in the previously cited references.

In the current procedure, the microphone signals were acquired over 39 s at a 51,200 Hz sampling rate by an array of 62 microphones designed as a modified Archimedean spiral. The microphones were GRAS 46BD 1/4 in., and the acoustic data-acquisition systems were based on National Instruments hardware. Frequencies were divided into bands with different resolutions along the frequency range of interest; therefore, different lengths of data blocks were employed (Table 2).

As shown in Fig. 2, the array is mounted in a position from which it focuses the wing model lower surface. A mesh subdomain named the region of interest (ROI) is defined for the evaluation of the noise spectra from the array measurements. Figure 3 shows the array (filled circles), the positions and dimensions of the mesh (dotted line rectangle), and the ROI (dashed line rectangle) relative to the projection of the model (slat, main element, and flap; continuous lines) on the array plan at a 4 deg angle of attack.

The ROI was located 850 mm from the microphone array; it measured 800 mm in the spanwise direction and 180 mm in the streamwise direction. Such values were obtained from tests that showed a good compromise between regions sufficiently large for the inclusion of the bulk of the source and sufficiently small for the avoidance of side lobes and residual three-dimensional effects associated with model ends [7,23]. The spatial mesh used in the calculation of beamforming maps was contained in a rectangular domain. To account for the source energy spread at lower frequencies, the grid extents were twice as large as the array beamwidth. As the frequency increased, the energy spread reduced and the domain reduced accordingly. This reduction was
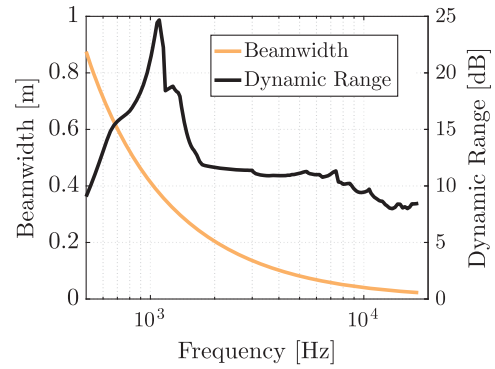
limited to 1400 mm in the spanwise direction and 300 mm in the chordwise direction. Tests were conducted to ensure the results' independence of the grid domain, which was centered around the ROI.

The array beamwidth was evaluated for the frequency range of interest as the diameter of the point spread function main lobe 3 dB below its peak; Fig. 4 shows the beamwidth as a function of frequency. The figure also shows the array dynamic range, evaluated as the difference between the peaks of the point spread function main lobe and the associated highest side lobe at each frequency. Both array parameters were evaluated for a plan distanced 850 mm from the microphones array plan.

1. Phased Microphone Array Techniques Employed

The frequency-domain beamforming formulation used here can be represented by

$$b(\boldsymbol{r}_s, \omega_l) = \boldsymbol{h}(\boldsymbol{r}, \omega_l)\mathbf{C}(\omega_l)\boldsymbol{h}(\boldsymbol{r}, \omega_l) \qquad (1)$$

where $b(\boldsymbol{r}_s, \omega_l)$ is a squared pressure estimate obtained by the algorithmic steering of the array beam toward a focal point located at position $\boldsymbol{r}_s$ relative to a reference point $\boldsymbol{o}$ on the array surface. Vector $\boldsymbol{r}$ gathers the distances from the focal point to each array microphone. The cross-spectral matrix $\boldsymbol{C}(\omega_l)$ contains all auto- and cross spectra of the signals measured by the array at frequency ω_l. The steering vector $\boldsymbol{h}(\boldsymbol{r}, \omega_l)$ is a complex-valued column vector that associates the focal point with each array microphone, and the symbol † designates the Hermitian operator. The steering vector component for an arbitrary microphone of index m is given by

$$h_m(\boldsymbol{r}_m, \omega_l) = \frac{g_m(\boldsymbol{r}_m, \omega_l)}{\sqrt{\sum_{n=1}^{M} \sum_{m=1}^{M} |g_m||g_n|}} \qquad (2)$$

where M is the total number of microphones, and $g_m(\boldsymbol{r}_m, \omega_l)$ is the transfer function $(1/r_m)e^{-i\omega_l(r_m)/c}$ that models the sound wave received by the mth array microphone due to a unitary monopole source distanced $r_m = |\boldsymbol{r}_m|$ from it. The source-to-microphone transfer function is then normalized by the transfer function that models the sound wave received at the array reference point $(1/r_s)e^{-i\omega_l(r_s)/c}$, which leads to

$$g_m(\boldsymbol{r}_m, \omega_l) = \frac{r_s}{r_m}e^{-i\omega_l(r_m-r_s)/c} \qquad (3)$$

Equation (3) holds for a situation in which the medium, source, and listener (microphone) are stationary with respect to the same reference frame. In a wind tunnel, the microphones and sources are stationary, whereas the flowfield drags the wave front downstream and produces a convective effect that requires a proper correction for the avoidance of misinterpretation of a source position. The correction was accomplished through Eq. (3) for the effective distance along which the sound moved with respect to the medium [35].

Table 2 Discretization of the narrowband frequencies employed for PSD estimations

Frequency range, kHz	Frequency resolution, Hz	Number of blocks
0.50–1.60	25	1,947
1.65–3.20	50	3,895
3.30–6.40	100	7,791
6.60–12.80	200	15,584
13.20–25.20	400	31,170

Insertion of Eq. (2) into Eq. (1) and application of the required matrix products yield

$$b(\boldsymbol{r}_s, \omega_l) = \frac{|\sum_{n=1,n\neq m}^{M}\sum_{m=1,m\neq n}^{M}(g_m^*)[C_{m,n}](g_n)|}{\sum_{n=1,n\neq m}^{M}\sum_{m=1,m\neq n}^{M}|g_m||g_n|} \quad (4)$$

where the dependence on the vector position and frequency was discarded for simplicity of notation, and the symbol * denotes the complex conjugate. $C_{m,n}$ denotes the cross spectrum between microphones m and n, and condition $m \neq n$ indicates the cross-spectral matrix main diagonal elements were discarded in the summation [33]. Equation (4) shows the conventional beamforming formulation as a weighted sum in which the microphone cross spectra were weighted by complex-valued g_m^* aiming at a proper signal phase delay and scaling toward a reference level. Equation (4) can separate signals from different locations and behaves as a directional sound receiver for which the performance is ultimately governed by the steering vector definition [34]. If a grid of points is constructed to cover a region of interest for the mapping of acoustic sources, Eq. (4) is applied to provide a source amplitude estimate at each grid point, generating a source image map at each spectral frequency from which the sound pressure level associated with a distributed source can be calculated by a simple spatial integration [36].

2. Beamforming Output Enhancement by Array Shading

Some studies [7] present a good agreement between experimental and numerical slat noise results. However, in this reference, at higher frequencies, the agreement was not as good and the experimental results provided lower estimates than the numerical ones. Underestimation of high-frequency acoustic levels has been associated with loss of coherence over the microphone array [27]. This problem would be particularly relevant for wind-tunnel wall-mounted microphones owing to the turbulent boundary that develops over the array. In the current study, the high-frequency content at higher angles of attack may be relevant; therefore, an attempt was made to improve the experimental estimates at higher frequencies.

Array shading approaches have been successfully employed to control the loss of coherence over the array [37,38]. The idea is to reduce the array aperture for higher frequencies; therefore, the loss of coherence would be lower because only microphones close to each other were considered.

Array shading can be included in the conventional beamforming formulation if an additional weighting factor w is introduced for each microphone according to

$$\boldsymbol{h}_w = \begin{bmatrix} h_1 w_1 \\ h_2 w_2 \\ \vdots \\ h_m w_m \\ \vdots \\ h_M w_M \end{bmatrix} \quad (5)$$

We extended the cluster approach [37], introducing an array shading methodology based on coherence among microphone signals. In this approach, a weighting factor w_m for a microphone of index m is defined as

$$w_m = \frac{1}{M-1}\sum_{n=1,n\neq m}^{M}\frac{[C_{m,n}]^2}{[C_{m,m}][C_{n,n}]} \quad (6)$$

where w_m is the mean coherence of the mth microphone signal with respect to the signals measured by the other array microphones as a function of frequency ω_l. By inserting Eq. (5) into Eq. (4) and using Eq. (6), the cross-spectra terms representing signals with a high mean coherence level were overweighted, whereas those of a low mean coherence level were underweighted. The normalization adopted in Eq. (4) ensures the weighting factors lead to no artificial array output gain. As the cross-spectral matrix results from the averaging of a large number of data blocks, the strategy is expected to increase the contribution of signals that remain highly correlated after the ensemble averaging and reduce the contribution of poorly correlated signal pairs.

C. Numerical Simulations

Numerical simulations were conducted for the study of the flow behavior around the airfoil and its relation to the acoustic experimental data. OpenFOAM software (simpleFoam package, for which an open-source popular computational fluid dynamics code is readily available on the Internet) was employed for obtaining the mean flow around the airfoil. The Spalart–Allmaras turbulence model was used. A 1700 mm computational domain, perpendicular to the flow direction, was defined to reproduce the wind-tunnel conditions. In the streamwise direction, after a domain independence test, the extension was fixed at 10 and 11 chords upstream and downstream of the airfoil, respectively. The Mach and Reynolds numbers employed were 0.1 and 9.62×10^5, respectively. The results of the mesh independence tests are shown in Fig. 5 for the baseline geometry at 0 deg (the noisiest case) and 16 deg angles of attack (the expected most critical case for domain independence). The remaining differences on the pressure distribution were considered insignificant. The chosen mesh had the least refined grid and smallest streamwise domain from those shown. Figure 6 displays the final domain and mesh used for all cases simulated.

III. Results

A. Pressure Coefficient

Figure 7 shows the chordwise pressure distributions c_p for the selected angles of attack, 34 m/s freestream speed, and baseline configuration. A good agreement between numerical and experimental results was obtained for the positive angles of attack (Fig. 7a); however, for the negative angles of attack (Fig. 7b), the agreement was not as good. Between −2 and −4 deg, the experimental data showed a drastic fall in lift, which was captured
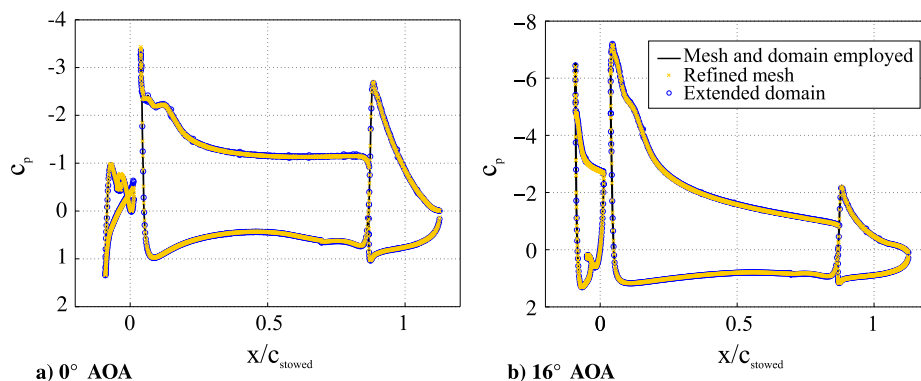

a) 0° AOA

b) 16° AOA

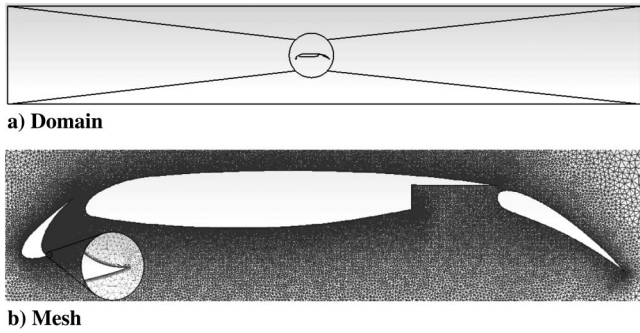Fig. 5 Domain and mesh independence analysis.

a) Domain

b) Mesh

Fig. 6 Final domain and mesh employed in the numerical simulations.

a) Positive angles of attack   b) Negative angles of attack

Fig. 8 Chordwise pressure coefficient distribution on the slat for the baseline configuration.

only for angles of attack below −4 deg in the numerical simulations. Such disagreement is addressed in Sec. III.E.

Figure 8 zooms in on the slat c_p distribution of Fig. 7. Numerical and experimental results are shown. For the cove surface, dashed lines (numerical results) and open symbols (experimental) are employed. The pressure measurements in the slat cove were difficult, in particular, for negative angles of attack for which the flow is very complex (as will be shown later in Sec. III.E) and c_p is very close to zero, and hence more vulnerable to uncertainties. The pressure on the upper surface of the slat, which is more relevant, shows a fair agreement with the numerical results: in particular, for lower angles of attack.

Figures 9a–9e compare, for selected angles of attack, the chordwise pressure distributions for the baseline, D35, and G206OL160 configurations. As the angle of attack increases, the lift increases for the slat and the main element and is reduced for the flap, which is the expected behavior of a three-element high-lift configuration. Figure 9f shows the lift dependence on the angle of attack for the three configurations. Poststall results are not shown; however, the highest angle of attack displayed corresponds to the maximum lift for each configuration, within a 2 deg discretization. The slat is designed to increase the lift by increasing the stall angle of attack. Its main effect is the reduction of the main element suction peak. The D35 configuration is less efficient because it exhibits a higher suction peak than that of the baseline. Accordingly, it stalls at approximately 16 deg, whereas the baseline configuration stalls at 18 deg. The stall of the G206OL160 configuration is similar to that of the baseline; however, at lower angles of attack (say 6 deg), it produces a lower lift and a more negative pitching moment, which are undesirable effects. The more negative pitching moment of the G206OL160 configuration is seen by the fact that, close to its leading edge, the main element is much less loaded than for the other configurations. This is an important characteristic because the normal operation of a high-lift system often ranges between 4 and 8 deg. The results are consistent with the optimized character of the baseline MD30P30N design. The configurations here tested were selected
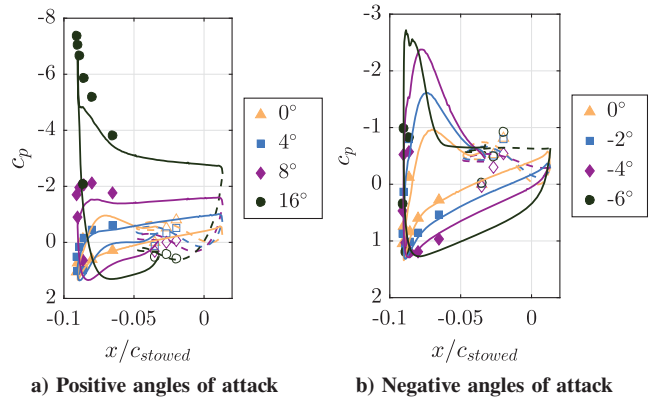
from [7], in which several slat configurations were studied at angles of attack ranging from 2 to 10 deg. The results suggest good aerodynamics performance is often associated with high slat noise at operational angles of attack. The D35 and G206OL160 configurations were chosen because they represent two different types of poor slat performance, namely, limited reduction of the main element suction peak at high angles of attack and poor lift and pitching moment (and possibly drag) performances at operational angles of attack. The idea was to investigate whether they could represent two different slat noise behaviors.

Figures 7 and 9a–9e show a step on the c_p pressure side. The step position did not change with the model configuration nor the angle of attack. Moreover, it was not observed in the numerical simulations. At the same time, it could not be associated with any model surface irregularity. The model employed a number of scanning valve systems, and it is possible this feature laid where groups of pressure tappings were separated into two different scanning systems. This is consistent with the pressure step being within the nominal measurement uncertainty stated for those instruments, which was somewhat large for this pressure levels in view of the high-pressure range required for stall measurements. Unfortunately, this aspect can no longer be traced because the scanning valve systems have been removed from the model. In any case, it is considered that this aspect affected neither the slat sound emission nor the interpretation of the results.

Figure 10 shows the pressure distribution along the span obtained with the use of wind-tunnel wall boundary-layer suction [7]. The results indicate that, within the ROI, a fairly uniform pressure along the span was obtained, even at relatively high angles of attack.

B. Noise Spectra

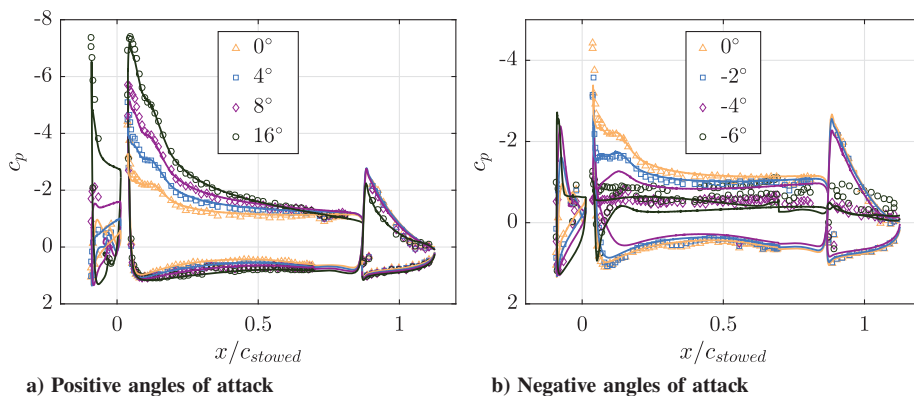The weighting approach was tested for the conventional beamforming, CLEAN-SC, and DAMAS deconvolution algorithms.

a) Positive angles of attack   b) Negative angles of attack

Fig. 7 Numerical and experimental results of chordwise pressure distribution c_p.
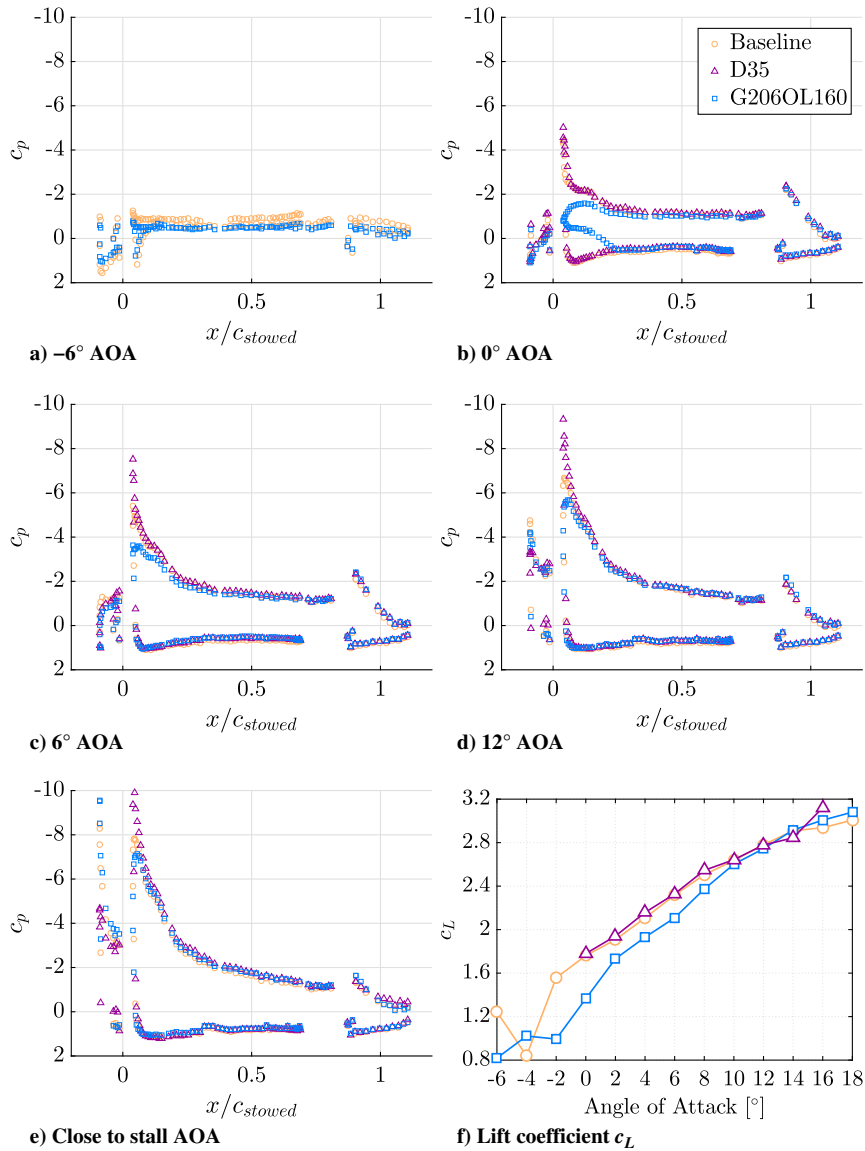
Fig. 9 Experimental chordwise pressure distribution and lift coefficient for the three slat configurations tested.

Such an approach had a small impact on the CLEAN-SC results, and the conventional beamforming results were not as good as those of DAMAS. In what follows, results from CLEAN-SC, DAMAS, and DAMAS in combination with the coherence weighted approach (hereinafter referred to as DAMAS-CW) are compared for assessment of the improvement obtained.

Figure 11 shows the noise spectra for selected angles of attack. The figure also shows two indications of the wind-tunnel background noise level, namely, the microphone autospectra averaged over all microphones and the spectra obtained through integration of the noise sources over the ROI for the empty wind tunnel operating at $U_\infty = 34$ m/s. The slat noise approached the empty tunnel noise for extreme angles of attack. Often, CLEAN-SC provided higher spectral levels. However, it yielded no slat noise estimates at some portions of the spectra: in particular, where it approached the background noise. In general, DAMAS-CW provided higher spectral estimates than regular DAMAS throughout the frequency range (in particular, at higher frequencies) and did not suffer from the shortcomings observed for CLEAN-SC.

Figures 12 and 13 display source maps obtained by conventional beamforming, CLEAN-SC, regular DAMAS, and DAMAS-CW, respectively, for 1175 Hz (the second tonal peak of the low-frequency

narrowband peak slat noise component), and 10,400 Hz (the high-frequency hump slat noise component) for the baseline configuration at a 2 deg angle of attack. Conventional beamforming displays a wide source representation, even at high frequencies, whereas CLEAN-SC provides a segmented source. DAMAS-CW generated the best line source representation distributed along the slat span, which was slightly better than regular DAMAS.

It is interesting to note the brackets may act as an important localized source; Figs. 12 and 13 do not show a clear indication of such a feature. Moreover, the source maps indicate no relevant source associated with either model end effects or the suction employed for the wind-tunnel wall boundary-layer control. Previous experiments [7,23], which employed the same experimental setup, addressed this issue in more detail. Such studies employed the same ROI as ours and showed the wind-tunnel wall suction, the model effect, and the brackets did not significantly affect the results.

Figure 14 shows the weighting distribution over the array for a selected case, i.e., baseline configuration, $U_\infty = 34$ m/s, and 6 deg AOA. As the frequency increases, a smaller portion of the array is heavily weighted. The picture shows the great adaptability of the approach with respect to the microphones used and only a mild tendency of the central portion of the array toward being heavily
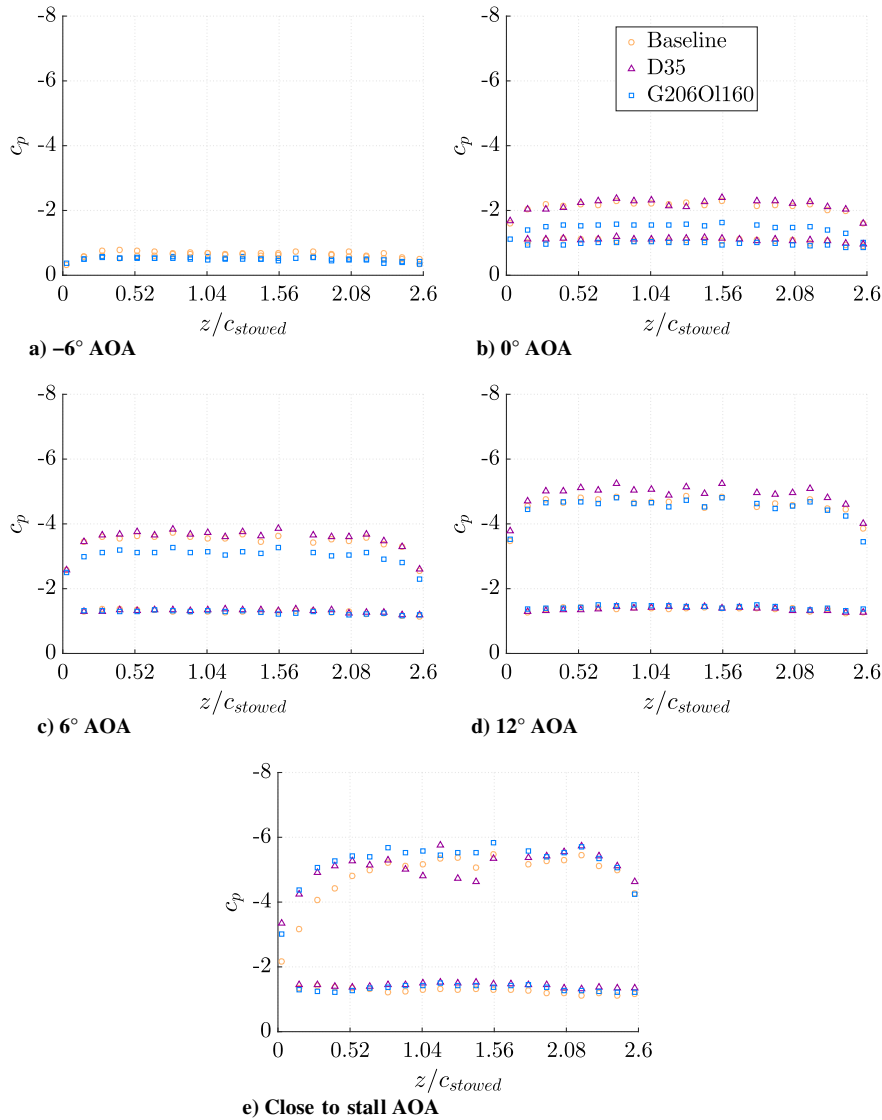
a) −6° AOA

b) 0° AOA

c) 6° AOA

d) 12° AOA

e) Close to stall AOA

Fig. 10   Experimental spanwise pressure distribution for the three slat configurations tested.

weighted at higher frequencies. The flexibility and adaptability of DAMAS-CW approach seem to represent an improvement over the original cluster approach [37] from which it derives.

The results suggest DAMAS-CW provided a good combination of the higher spectral estimates from CLEAN-SC and the better source representation obtained from regular DAMAS. Therefore, the method was employed for the analysis of all data collected in the experimental campaign.

Figure 15 shows noise spectra results for baseline, D35, and G206OL160 geometrical configurations for $U_\infty = 34$ m/s. Only the baseline and G206OL160 configurations were tested for angles of attack below 0 deg. The noise spectra for such lower angles are broadband-like, and their intensity levels are close to that of the empty wind tunnel. The slat noise components of multiple narrowband peaks of low-frequency and high-frequency broadband peaks are present at a 0 deg angle of attack. At 6 deg, the low-frequency narrowband peaks are reduced and the high-frequency broadband component increases. For higher angles of attack (i.e., above 12 deg), the multiple narrowband peaks are suppressed and the slat noise approaches the empty wind-tunnel background noise. The high-frequency broadband hump seems to reduce its intensity level as the angle of attack increases from 6 deg, whereas the frequency of the hump increases. However, this observation must be taken with care because this spectral range is close to our top spectral limit: i.e., 25.2 kHz. Narrowband signals, not reported in the literature, are present at

0 deg midfrequencies and for angles of attack close to stall at high frequencies. Such signals are regarded as spurious noise and will be addressed later.

The contour plots in Fig. 16 show the spectra variation for all angles of attack measured. The picture provides a more complete view of the main tendencies of noise variation with angles of attack. The only salient spectral signatures are the high-frequency hump and the low-frequency narrowband peaks. The low-frequency narrowband peaks are most intense at 0 deg, sharply decay as the angle of attack is reduced, and gradually decay as the angle of attack is increased. The frequencies of the low-frequency narrowband peaks do not vary substantially as a function of the angle of attack. The high-frequency hump is not very intense, although it is relatively more important for the D35 configuration. Its maximum contribution occurs for angles of attack between 4 and 10 deg, and its frequency increases with the angle of attack.

C. Overall Sound Pressure Level

Figure 17 shows the overall sound pressure level (OASPL) over the frequency range of interest (500 Hz to 25.2 kHz) as a function of the angle-of-attack for all slat geometrical configurations tested at a 34 m/s freestream speed. The OASPL is clearly dominated by the low-frequency narrowband peaks. For all configurations, the noisiest angle of attack is 0 deg. The OASPL decays sharply as the angle of attack reduces and gradually as it increases from 0 deg. The noisiest
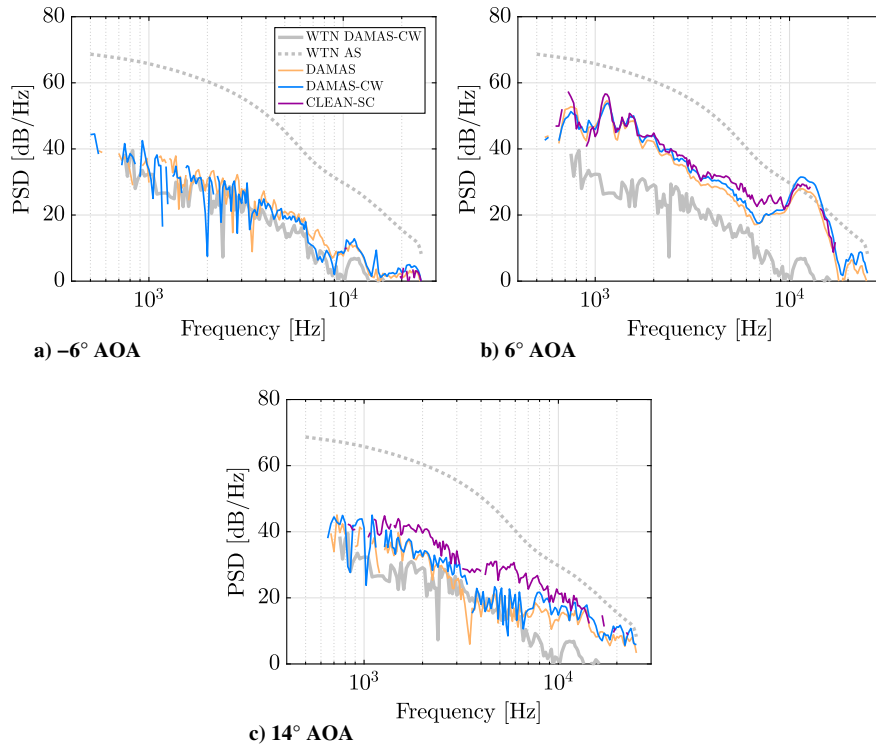
a) −6° AOA   b) 6° AOA

c) 14° AOA

Fig. 11   Comparison of baseline configuration noise spectra for different beamforming procedures.

a) CBF   b) CLEAN-SC   c) DAMAS   d) DAMAS-CW
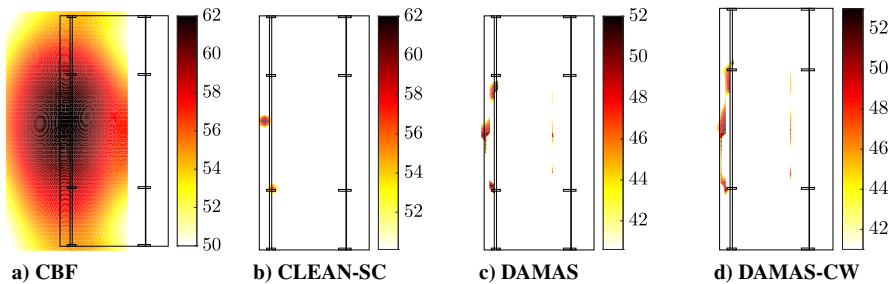
Fig. 12   Baseline configuration noise source maps at 1175 Hz frequency for different beamforming procedures.

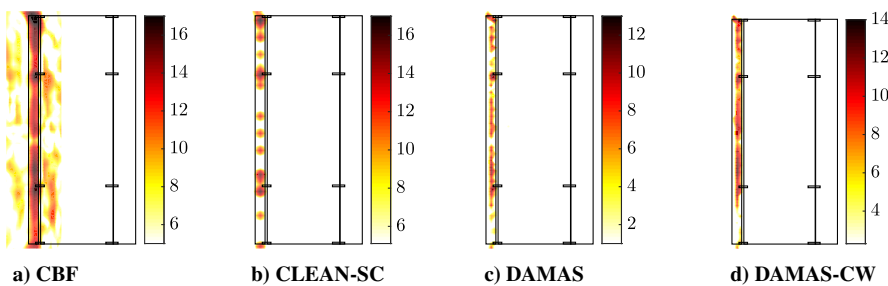a) CBF   b) CLEAN-SC   c) DAMAS   d) DAMAS-CW

Fig. 13   Baseline configuration noise source maps at 10,400 Hz frequency for different beamforming procedures.

configuration is the baseline for the entire range of angles of attack tested, except for very high angles of attack, at which configuration D35 is slightly noisier. Remarkably, the baseline is approximately 8 dB noisier than the other configurations for a 0 deg angle of attack. It illustrates how much good aerodynamic performance is accompanied by higher noise. The analysis reveals the sound variation with respect to angle of attack is not very sensitive to the

model configuration; only the intensity level is more strongly affected.

The symbols in Fig. 17 refer to the dominant low-frequency narrowband peak for each configuration between −2 and 8 deg angles of attack, as the peaks are ill defined outside this range. The analysis shows a significant variation in the dominant peak. The baseline seems to favor the second peak, whereas G206OL160 and D35
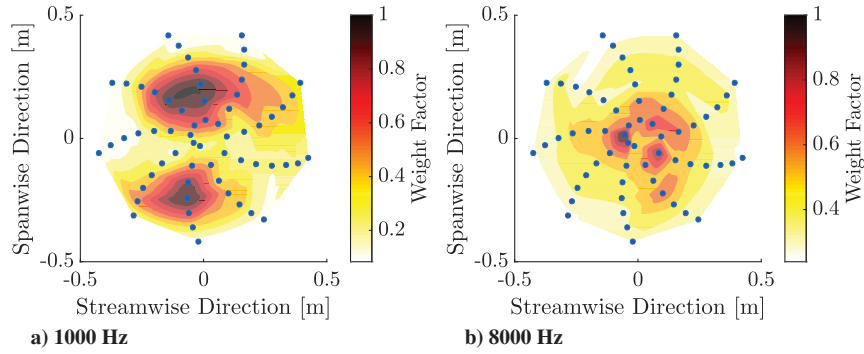
a) 1000 Hz **b) 8000 Hz**

Fig. 14 Weighting vectors w_m distribution over the microphones array applied to DAMAS-CW.

a) −6° AOA **b) 0° AOA**

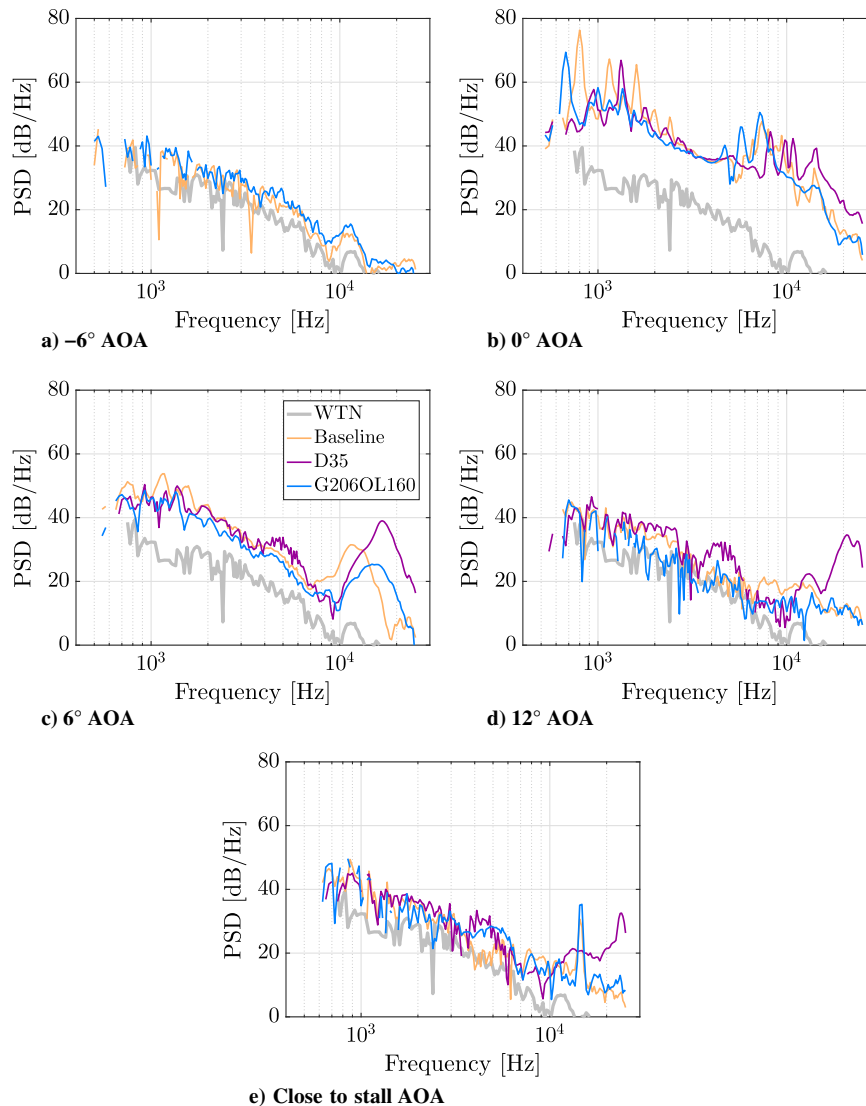**c) 6° AOA** **d) 12° AOA**

e) Close to stall AOA

Fig. 15 Noise spectra for the three slat configurations tested.

configurations favor the first and third peaks, respectively. The peak dominance also depends on the angle of attack, with the first peak tending to dominate at higher angles of attack.

D. Dependence of the Slat Noise on the Mach Number

Figure 18 shows noise dependence on the Mach number for the OASPL computed in the 500 to 25,200 Hz frequency range, which covers the entire relevant signal for all angles of attack,

configurations and freestream speeds tested. The wind-tunnel noise is represented by the horizontal straight lines. The OASPL scaling was employed to summarize in one plot all the angles of attack and slat configurations covered, offering an indication of how the dominant source scales with the Mach number at each angle of attack and configuration. In doing so, it was possible to establish some regimes of Mach scaling. Results are shown for the fifth and eighth Mach power scaling, only for the baseline configuration. For the baseline,
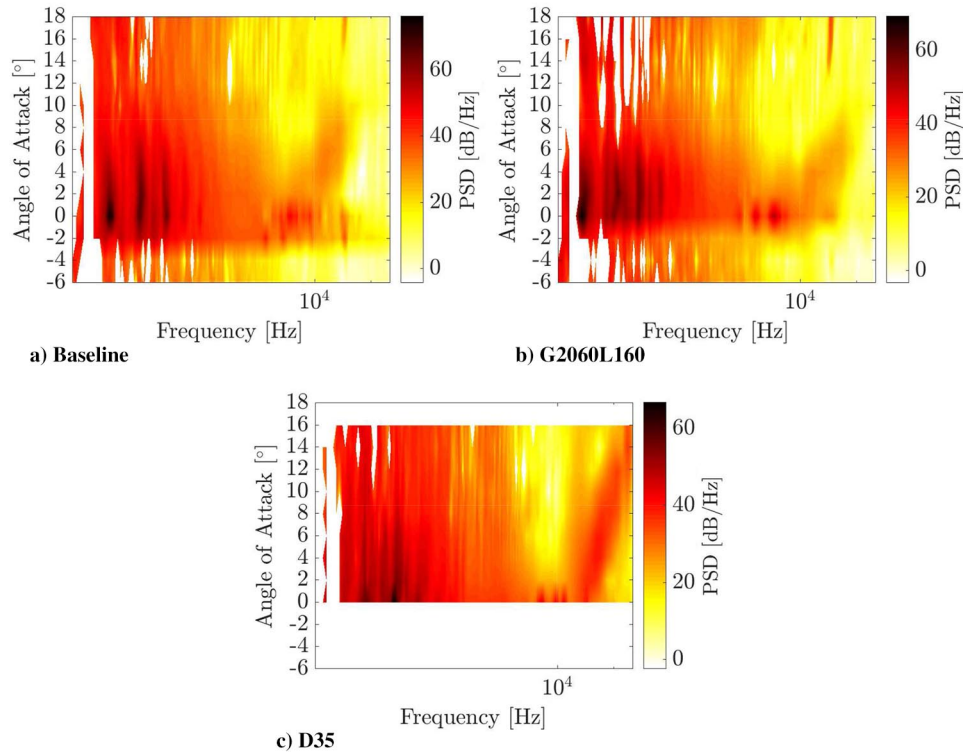
Fig. 16   Power spectral density for the three slat configurations tested.
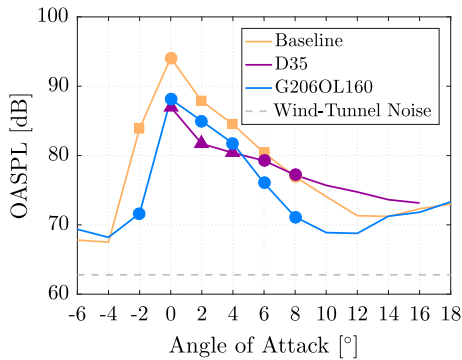

Fig. 17   Slat noise overall sound pressure level for the three slat configurations tested.

the fifth power is reasonable at higher angles of attack; however, lower angles of attack required a much higher Mach power. A similar, albeit less salient, situation is observed for the G206OL160 configuration (Fig. 18c). For the D35 configuration (Fig. 18d), the fifth Mach power also does not provide a good collapse. Interestingly, the wind-tunnel background noise collapses very well for such a Mach power. Clearly, a single Mach power is not suitable for the OASPL scaling of the configurations and angles of attack covered. Moreover, for a given configuration, the higher OASPL noise levels may scale to a Mach power well above five.

The Mach number effect becomes more specific if the analysis considers the noise spectra. Figure 19 shows scaled and unscaled spectral results for the baseline configuration. The scaled horizontal coordinate uses the Strouhal number based on the slat chord and the freestream velocity. The vertical coordinate shows the power spectral density (PSD) levels adjusted to a fifth power of Mach the number [10]. Unscaled results are given for reference.

At a 0 deg angle of attack, the low-frequency narrowband peaks dominate; whereas at 8 deg, the high-frequency hump is more

relevant; and at 18 deg, the noise is very low. A very good collapse on the fifth power of the Mach number was observed for certain regions of the spectra and angles of attack, i.e., the midfrequencies at 0 deg and the low to midfrequencies at 8 deg. For other spectral regions, the collapse is only fair, such as the high-frequency hump at 8 deg and almost the entire spectra for 18 deg. Nevertheless, the noisiest component (the low-frequency narrowband peaks) clearly scaled to a much higher power of the Mach number.

Figure 20 shows Strouhal and Mach number collapses for G206OL160 and D35 configurations, respectively. As for the baseline in Fig. 19, the angles of attack were chosen to illustrate the general features of the spectra. Again, a fifth power of the Mach number was employed for reference. The spectral pattern of configuration G206OL160 is similar to that of baseline, although the high sensitivity of the low-frequency narrowband peaks with respect to the Mach number is less salient. Configuration D35 shows a good fifth-power collapse for the low and midfrequencies, where the spectra is essentially broadband. However, at 10 deg, where the high-frequency hump is most clearly observed, the spectrum seems to scale to a lower power of Mach. In general, the spectra conformed to a Strouhal number scaling, with a few exceptions that will be addressed in the following.

The high sensitivity of the low-frequency narrowband peaks with respect to the Mach number is consistent with Fig. 18 where, for angles of attack for which the noise spectra are dominated by the low-frequency narrowband peaks, the OASPL collapse requires a much higher Mach power. The lower sensitivity of the high-frequency hump with respect to the Mach number is also consistent with Fig. 18, which shows, at high angles of attack, the noise from the D35 configuration scales to a Mach power lower than the fifth. Overall, the results indicate different source mechanisms in the slat may scale to different powers of Mach. Because different mechanisms prevail for different configurations and angles of attack, a single Mach power is unsuitable for all configurations and angle-of-attack ranges. In the operational angle-of-attack range, a power between four and six may provide a reasonable collapse; however, the extended data discussed here place this aspect in a different perspective. In particular, the very
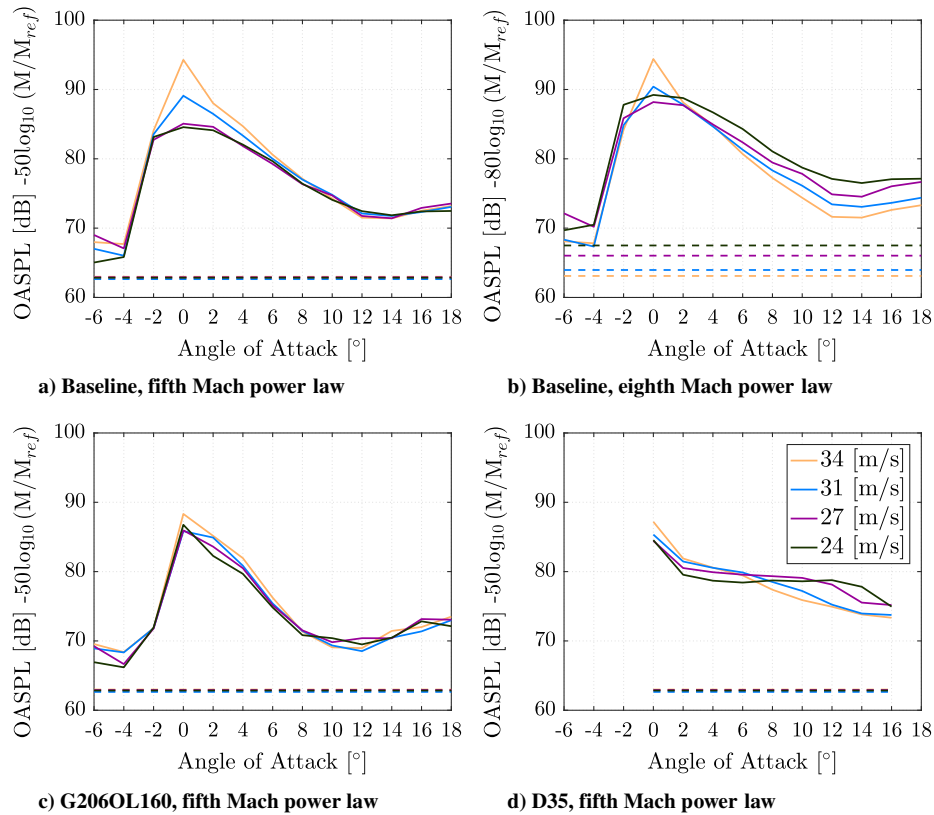
a) **Baseline, fifth Mach power law**

b) **Baseline, eighth Mach power law**

c) **G206OL160, fifth Mach power law**

d) **D35, fifth Mach power law**

Fig. 18   Overall sound pressure level Mach number collapses for the three slat configurations tested.

sensitivity of the low-frequency narrowband peaks is remarkable and has not been previously reported in the literature.

The narrowband peak components have been associated with a feedback process by which vortices impinge the slat cove, emitting acoustic waves that travel and excite new vortices at the slat cusp [39]. If such a feedback mechanism occurs, the strong dependence on Mach number could be explained. The transfer of energy from the vortices to the sound wave may scale at Mach to the (say) fifth power. However, in a feedback process, the vortices would become stronger if excited by stronger acoustic waves. In such a system, both the transfer of energy into acoustic waves and the source itself would be enhanced as the Mach number increased, which would clearly lead to much stronger Mach number sensitivity than the one expected with no feedback loop. Hence, the results support the existence of a feedback loop mechanism associated with a low-frequency acoustic narrowband peak observed in the slat cove.

Three spectral features (i.e., a region in the 6 to 10 kHz frequency range) at moderate positive angles of attack, a region between 5 and 10 kHz at a 0 deg angle of attack, and a narrowband peak at approximately 15 kHz showed poor collapse on the Strouhal scale. All configurations tested, except configuration D35 at the 15 kHz narrowband peak, exhibited such features, which collapsed on the frequency scale. The first feature has been reported [7], although it is not relevant because it corresponds to a very low noise level. The others have not been reported elsewhere. Figure 21 shows noise source maps belonging to these two spectral regions. They contain only localized point sources, which do not seem to represent a genuine source of the two-dimensional slat. Owing to their frequency scaling, absence of previous reports, and position in space, these two sources were considered spurious and possibly associated with model imperfections and/or structural resonance. They were very weak relative to the dominant slat sources and did not affect the results.

E. Velocity Field

According to the numerical simulations, for positive angles of attack, the position of the attaching point moves farther from the

airfoil trailing edge as the angle of attack increases: from approximately 13% of the slat chord at a 0 deg angle of attack to around 32% at 16 deg (Figs. 22a–22c), which shrinks the recirculating region inside the slat cove. The attachment point is located where the dividing streamline (the one separating the flow in the bubble and the flow that passes through the slat gap) reaches the slat lower surface and forms a stagnation point. It is marked with an arrow in Figs. 22a–22c. According to the experimental results, the higher the angle of attack, the lower the slat noise radiated. Some studies considered the slat noise was ultimately caused by the interaction between the cove turbulence and the slat trailing edge. The higher turbulence intensity was found at the reattachment point on the lower surface of the slat [7]. If the slat noise was associated with the interaction of the turbulence with the slat trailing edge, the gradually larger distance between the reattachment point and the slat trailing edge for higher angles of attack was possibly related to the noise reduction.

For negative angles of attack, the streamline plots show a different scenario for the flow around the airfoil (Figs. 22d–22f). In the 0 to −4 deg range of angles of attack, the slat recirculation bubble deforms as the angle of attack decreases, producing a longer mixing layer path. Nevertheless, the reattachment point does not move significantly from that of a 0 deg angle of attack. The longer mixing layer may provide a less coherent flow at the reattachment point that can be related to the reduction of the magnitude of low-frequency narrowband peaks.

For even lower angles of attack, a stagnation point is formed on the upper surface of the main element and the slat gap flow changes its direction. In fact, this is a drastic flow modification that occurs very sharply as the angle of attack is reduced. Figures 22g–22i show results for the baseline geometry and angles of attack between −4.8 and −5 deg. A counter-rotating bubble is formed in the slat cove, which displaces the original bubble to a region below the airfoil main element.

The disagreement in the angle of attack for which the loss of lift is observed in the experimental and numerical results is related to the fact that the phenomenon is very abrupt. On the one hand, owing to
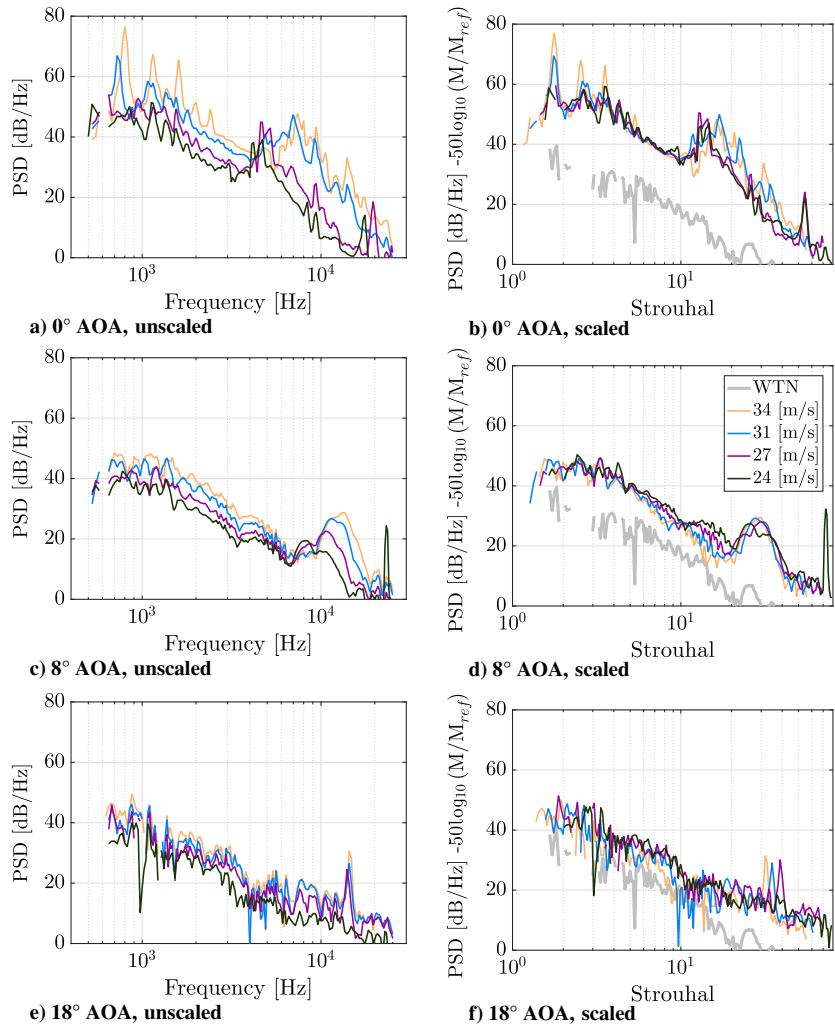
a) 0° AOA, unscaled
b) 0° AOA, scaled
c) 8° AOA, unscaled
d) 8° AOA, scaled
e) 18° AOA, unscaled
f) 18° AOA, scaled

Fig. 19 Mach and Strouhal number noise spectrum scaling for the baseline configuration.

a) G206OL160 configuration, 2° AOA
b) G206OL160 configuration, 10° AOA
c) D35 configuration, 2° AOA
d) D35 configuration, 10° AOA
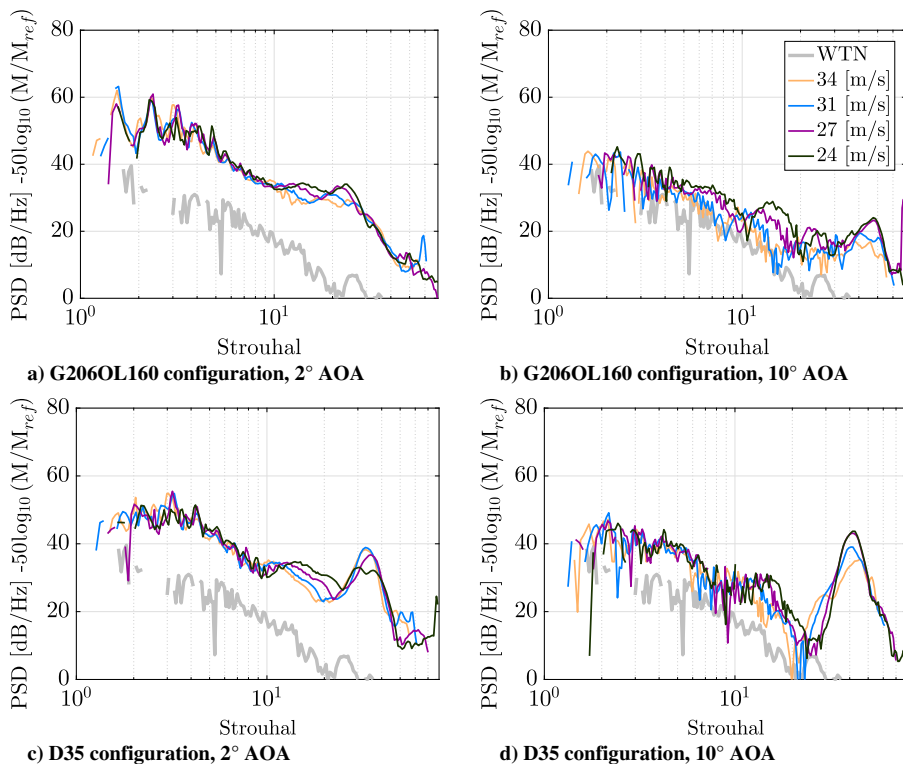
Fig. 20 Mach and Strouhal number noise spectrum scaling for G206OL160 and D35 configurations.

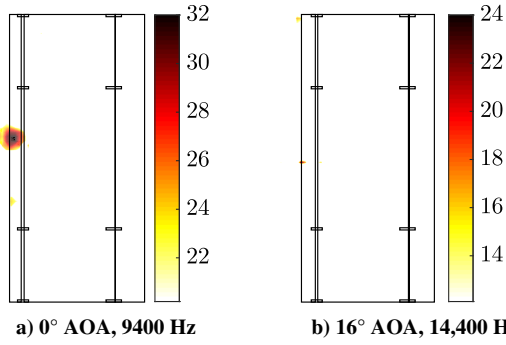**a) 0° AOA, 9400 Hz**   **b) 16° AOA, 14,400 Hz**

Fig. 21   DAMAS-CW noise source maps at frequencies corresponding to spurious peaks in the noise spectra.

the limited angle-of-attack discretization in the experiment, the exact angle of attack for which the phenomenon is observed is not precisely determined and may be very close to −4 deg. On the other hand, close to the condition of the abrupt lift loss, the base flow is likely to be very sensitive to small variations, and even hysteresis may be present. Under such circumstances, a perfect agreement is difficult to reach between numerical and experimental results (or even between different experimental results). Therefore, the good agreement at angles of attack just above the sudden lift loss and the fair agreement for angles of attack just below it can be considered satisfactory. Although, in a real airplane, the effective angle of attack may change along the wingspan, the slat device is never expected to operate under those conditions. The results for such angles of attack are discussed in the paper, only to ensure the whole slat operating regime is covered.

No significant differences were observed for the angle-of-attack effect on the velocity field for the baseline, G206OL160, and D35 configurations. The angle of attack for the drastic flow modification at negative angles of attack is slightly dependent on the slat geometrical parameters; however, the general behavior is the same for all geometries simulated.

IV.   Conclusions

This study has investigated the noise emission from the slat of an MD30P30N airfoil. The experimental acoustic data were obtained by a microphone array and processed by an in-house beamforming code. Numerical simulations of the mean flow around the airfoil were also carried out to help the interpretation of the results. The experimental and numerical pressure distributions on the airfoil surface agreed very well for positive angles of attack and satisfactorily for negative ones.

The investigation covered a −6 to 18 deg angle-of-attack range, i.e., below the minimum value for which the airfoil generates lift up to approximately the angle of stall. Two other design configurations of the MD30P30N airfoil [i.e., one with a smaller gap and overlap (G206OL160) and another with a higher slat deflection angle (D35)] were also included so that other possible regimes of slat noise could be investigated. The MD30P30N airfoil is a high-lift optimized configuration. As shown by the surface pressure distribution, the other configuration provided lower performance for both higher (D35) and operational angles of attack (G206OL160), respectively. The baseline configuration was the noisiest and confirmed previous conjectures that good aerodynamic performance was likely to be associated with high noise emission [23].
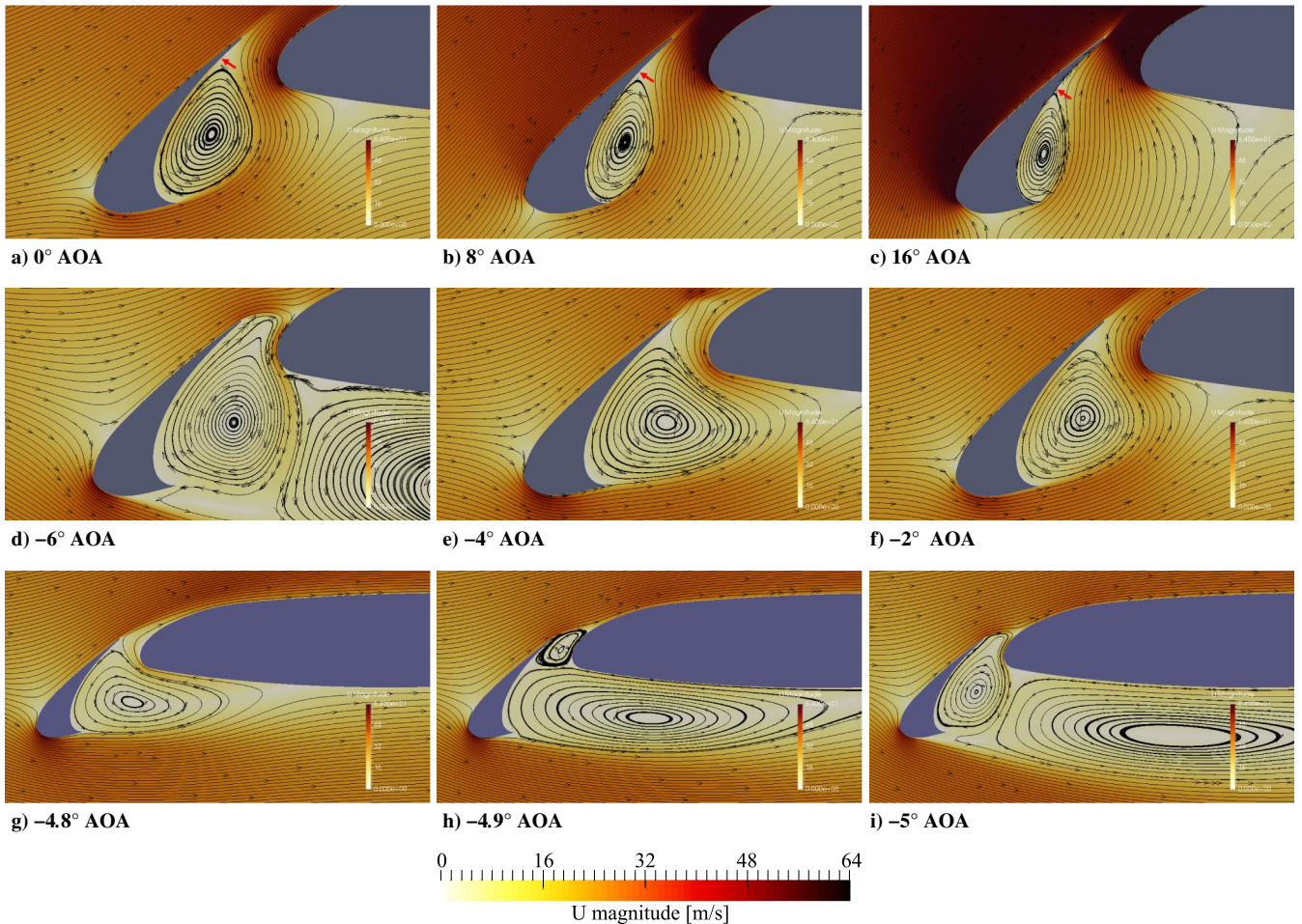

a) 0° AOA   **b) 8° AOA**   **c) 16° AOA**

d) −6° AOA   **e) −4° AOA**   **f) −2° AOA**

g) −4.8° AOA   **h) −4.9° AOA**   **i) −5° AOA**

0   16   32   48   64

U magnitude [m/s]

Fig. 22   Numerical simulations results of streamlines and velocity magnitude field for the baseline configuration.

Previous studies conducted by the same group [7] pointed to a beamforming underestimation of the noise at higher frequencies. Here, an array shading methodology based on microphone pair coherence was developed, and it improved both the high-frequency estimates and the source representation throughout the noise spectrum.

The dominant part of the spectra was the low-frequency range (with or without narrowband peaks) for all configurations and angles of attack of relevant noise, although the spectra included a midfrequency broadband and often a high-frequency hump. Such noise components were generally recognized in the slat noise spectra for scaled models tested under low Reynolds numbers. The results also showed the slat noise was below the wind-tunnel background level for angles of attack below −2 deg and above 12 deg, except for the largest slat deflection angle configuration that displayed a definite hump at higher frequencies up to stall. Overall, the results suggested the relevant noise mechanisms for slat noise were the ones already observed in the operational angle-of-attack range, namely, 2 to 10 deg.

For all configurations at a 0 deg angle of attack, the low-frequency range was dominated by narrowband peaks, which reduced gradually as the angle of attack increased. The numerical results showed the separation bubble in the slat cove shrank and the reattachment point moved away from the slat trailing edge as the angle of attack increased. The higher levels of turbulent activity were found at the reattachment point, and the results supported the association of the slat noise with the interaction of turbulence with the slat trailing edge.

The broadband slat noise spectra components scaled approximately at Mach to the fifth power, and the high-frequency hump seemed to scale to a lower power of the Mach number. The multiple low-frequency narrowband peaks showed a much stronger dependence on Mach number, above the 10th power for the highest peak levels, namely, close to 0 deg. The importance of narrowband peaks for real aircraft is still controversial. However, if such peaks prove their relevance, their scaling at such high Mach power will strongly impact the noise.

Acknowledgments

References

[1] Crighton, D., "Aeroacoustics of Flight Vehicles: Theory and Practice—Volume 1: Noise Sources," NASA WRDC-TR 90-3052, 1991.

[2] Dobrzynski, W., "Almost 40 Years of Airframe Noise Research: What Did We Achieve?" *Journal of Aircraft*, Vol. 47, No. 2, 2010, pp. 353–367.
doi:10.2514/1.44457

[3] Guo, Y., Yamamoto, K., and Stoker, R., "Component-Based Empirical Model for High-Lift System Noise Prediction," *Journal of Aircraft*, Vol. 40, No. 5, 2003, pp. 914–922.
doi:10.2514/2.6867

[4] Roger, M., and Perennes, S., "Low-Frequency Noise Sources in Two-Dimensional High-Lift Devices," *6th Aeroacoustics Conference and Exhibit, Aeroacoustics Conferences*, AIAA Paper 2000-1972, 2000.
doi:10.2514/6.2000-1972

[5] Manoha, E., Terracol, M., Lemoine, B., Griffon, L., and Garrec, L., "Slat Noise Measurement and Numerical Prediction in the VALIANT Programme," *18th AIAA/CEAS Aeroacoustics Conference (33rd AIAA Aeroacoustics Conference)*, AIAA Paper 2012-2100, 2012.

[6] Pascioni, K., Cattafesta, L. N., and Choudhari, M. M., "An Experimental Investigation of the 30P30N Multi-Element High-Lift Airfoil," *20th AIAA/CEAS Aeroacoustics Conference, AIAA Aviation*, AIAA Paper 2014-3062, 2014.

[7] Pagani, C. C., Jr., Souza, D. S., and Medeiros, M. A. F., "Slat Noise: Aeroacoustic Beamforming in Closed-Section Wind Tunnel with Numerical Comparison," *AIAA Journal*, Vol. 54, No. 7, 2016, pp. 2100–2115.
doi:10.2514/1.J054042

[8] Paschal, K., Jenkins, L., and Yao, C., "Unsteady Slat-Wake Characteristics of a High-Lift Configuration," *38th Aerospace Sciences Meeting and Exhibit*, AIAA Paper 2000-0139, 2000.

[9] Takeda, K., Ashcroft, G., Zhang, X., and Nelson, P., "Unsteady Aerodynamics of Slat Cove Flow in a High-Lift Device Configuration," *39th Aerospace Sciences Meeting and Exhibit*, AIAA Paper 2001-0706, 2001.

[10] Lockard, D. P., and Choudhari, M., "The Variation of Slat Noise with Mach and Reynolds Numbers," *17th AIAA/CEAS Aeroacoustics Conference (32nd AIAA Aeroacoustics Conference)*, AIAA Paper 2011-2910, 2011.

[11] Souza, D. S., Rodrguez, D., Simoes, L. G. C., and Medeiros, M. A. F., "Effect of an Excrescence in the Slat Cove: Flow-Field, Acoustic Radiation and Coherent Structures," *Aerospace Science and Technology*, Vol. 44, Instability and Control of Massively Separated Flows, July–Aug. 2015, pp. 108–115.
doi:10.1016/j.ast.2015.01.016

[12] Souza, D. S., Pagani, C. C., Jr., Rodrguez, D., and Medeiros, M. A. F., "Hydrodynamic Instability in the Generation of Slat Noise," *Procedia IUTAM*, Vol. 14, July 2015, pp. 344–353.
doi:10.1016/j.piutam.2015.03.058

[13] Chow, L., Mau, K., and Remy, H., "Landing Gears and High Lift Devices Airframe Noise Research," *8th AIAA/CEAS Aeroacoustics Conference and Exhibit*, AIAA Paper 2002-2408, 2002.

[14] Jenkins, L., Khorrami, M., and Choudhari, M., "Characterization of Unsteady Flow Structures Near Leading-Edge Slat: Part I: PIV Measurements," *10th AIAA/CEAS Aeroacoustics Conference*, AIAA Paper 2004-2801, 2004.

[15] Lockard, D. P., and Choudhari, M., "Noise Radiation from a Leading-Edge Slat," *15th AIAA/CEAS Aeroacoustics Conference (30th AIAA Aeroacoustics Conference)*, AIAA Paper 2009-3101, 2009.

[16] Murayama, M., Nakakita, K., Yamamoto, K., Ura, H., Ito, Y., and Choudhari, M. M., "Experimental Study on Slat Noise from 30P30N Three-Element High-Lift Airfoil at JAXA Hard-Wall Lowspeed Wind Tunnel," *20th AIAA/CEAS Aeroacoustics Conference, AIAA Aviation*, AIAA Paper 2014-2080, 2014.
doi:10.2514/6.2014-2080

[17] Khorrami, M. R., and Lockard, D. P., "Effects of Geometric Details on Slat Noise Generation and Propagation," *International Journal of Aeroacoustics*, Vol. 9, No. 4, 2010, pp. 655–678.
doi:10.1260/1475-472X.9.4-5.655

[18] Khorrami, M. R., Berkman, M. E., and Choudhari, M., "Unsteady Flow Computations of a Slat with a Blunt Trailing Edge," *AIAA Journal*, Vol. 38, No. 11, 2000, pp. 2050–2058.
doi:10.2514/2.892

[19] Choudhari, M. M., Lockard, D. P., Macaraeg, M. G., Singer, B. A., Streett, C. L., Neubert, G. R., Stoker, R. W., Underbrink, J. R., Berkman, M. E., and Khorrami, M. R., "Aeroacoustic Experiments in the Langley Low-Turbulence Pressure Tunnel," NASA TM 211432, 2002, pp. 1–46.

[20] Dobrzynski, W., and Pott-Pollenske, M., "Slat Noise Source Studies for Farfield Noise Prediction," *7th AIAA/CEAS Aeroacoustics Conference and Exhibit*, AIAA Paper 2001-2158, 2001.

[21] Guo, Y. P., and Joshi, M. C., "Noise Characteristics of Aircraft High Lift Systems," *AIAA Journal*, Vol. 41, No. 7, 2003, pp. 1247–1256.
doi:10.2514/2.2093

[22] Pott-Pollenske, M., Alvarez-Gonzalez, J., and Dobrzynski, W., "Effect of Slat Gap/Overlap on Farfield Radiated Noise," *9th AIAA/CEAS Aeroacoustics Conference and Exhibit*, AIAA Paper 2003-3228, 2003.

[23] Pagani, C. C., Jr., Souza, D. S., and Medeiros, M. A. F., "Experimental Investigation on the Effect of Slat Geometrical Configurations on Aerodynamic Noise," *Journal of Sound and Vibration*, Vol. 394, April 2017, pp. 256–279.
doi:10.1016/j.jsv.2017.01.013

[24] Dobrzynski, W., Nagakura, K., Gehlhar, B., and Buschbaum, A., "Airframe Noise Studies on Wings with Deployed High-Lift Devices," *4th AIAA/CEAS Aeroacoustics Conference*, AIAA Paper 1998-2337, 1998.

[25] Kolb, A., Faulhaber, P., Drobietz, R., and Grünewald, M., "Aeroacoustic Wind Tunnel Measurements on a 2-D High-Lift Configuration," *13th AIAA/CEAS Aeroacoustics Conference (28th AIAA Aeroacoustics Conference)*, AIAA Paper 2007-3447, 2007.

[26] Imamura, T., Ura, H., Yokokawa, Y., and Yamamoto, K., "A Far-Field Noise and Near-Field Unsteadiness of a Simplified High-Lift-Configuration Model (Slat)," *47th AIAA Aerospace Sciences Meeting Including The New Horizons Forum and Aerospace Exposition*, AIAA Paper 2009-1239, 2009.

[27] Sijtsma, P., "Acoustic Array Corrections for Coherence Loss due to the Wind Tunnel Shear Layer," *Proceedings on CD of the 2nd Berlin Beamforming Conference*, GFaI, Gesellschaft zur Förderung angewandter Informatik e.V. BeBeC-2008-15, 2008, pp. 1–10, http://www.bebec.eu/Downloads/BeBeC2008/Papers/BeBeC-2008-15_Sijtsma.pdf.

[28] Amaral, F. R., Himeno, F. H. T., Pagani, C. d. C., Jr., and Medeiros, M. A. F., "Experiments on Slat Noise from −6 to 18 Degrees Angles of Attack," *46th AIAA Fluid Dynamics Conference*, AIAA, Paper 2016-3629, 2016.

[29] Rumsey, C. L., Lee-Rausch, E. M., and Watson, R. D., "Three-Dimensional Effects in Multi-Element High-Lift Computations," *Computers and Fluids*, Vol. 32, No. 5, 2003, pp. 631–657.
doi:10.1016/S0045-7930(02)00032-4

[30] Amaral, F. R., Souza, D. S., Pagani, C. d. C., Jr., Himeno, F. H. T., and Medeiros, M. A. F., "Experimental Study of the Effect of a Small 2-D Excrescence Placed on the Slat Cove Surface of an Airfoil on its Acoustic Noise," *21st AIAA/CEAS Aeroacoustics Conference*, AIAA Paper 2015-3138 2015.

[31] Brooks, T. F., and Humphreys, W. M., "A Deconvolution Approach for the Mapping of Acoustic Sources (DAMAS) Determined from Phased Microphone Arrays," *Journal of Sound and Vibration*, Vol. 294, Nos. 4–5, 2006, pp. 856–879.

[32] Sijtsma, P., "CLEAN Based on Spatial Source Coherence," *International Journal of Aeroacoustics*, Vol. 6, No. 4, 2007, pp. 357–374.
doi:10.1260/147547207783359459

[33] Mueller, T. J., Allen, C. S., Blake, W. K., Dougherty, R. P., Lynch, D., Soderman, P. T., and Underbrink, J. R., *Aeroacoustic Measurements*, Springer, Berlin, 2002, pp. 62–97.

[34] Sarradj, E., "Three-Dimensional Acoustic Source Mapping with Different Beamforming Steering Vector Formulations," *Advances in Acoustics and Vibration*, Vol. 2012, June 2012, Paper 292695.
doi:10.1155/2012/292695

[35] Oerlemans, S., "Detection of Aeroacoustic Sound Sources on Aircraft and Wind Turbines," Ph.D. Thesis, Univ. of Twente, Enschede, The Netherlands, 2009.

[36] Brooks, T. F., and Humphreys, W. M., "Effect of Directional Array Size on the Measurement of Airframe Noise Components," *5th AIAA/CEAS Aeroacoustics Conference and Exhibit*, AIAA Paper 1999-1958, 1999.

[37] Brooks, T. F., Humphreys, W. M., and Plassman, G. E., "DAMAS Processing for a Phased Array Study in the NASA Langley Jet Noise Laboratory," *16th AIAA/CEAS Aeroacoustics Conference*, AIAA Paper 2010-3780, 2010.

[38] Sijtsma, P., "Phased Array Beamforming Applied to Wind Tunnel and Fly-Over Tests," SAE TP 2010-36-0514, Warrendale, PA, 2010.

[39] Terracol, M., Manoha, E., and Lemoine, B., "Investigation of the Unsteady Flow and Noise Sources Generation in a Slat Cove: Hybrid Zonal RANS/LES Simulation and Dedicated Experiment," *20th AIAA Computational Fluid Dynamics Conference*, AIAA Paper 2011-3203, 2011.

Y. Zhou
Associate Editor